Journal of
Applied Crystallography
ISSN 0021-8898

Received 16 August 2006
Accepted 7 March 2007

Phase behavior of platelet-shaped nanosilicate colloids in saline solutions – a small-angle X-ray scattering study

D. M. Fonseca,[a]* Y. Méheust,[a,d] J. O. Fossum,[a]* K. D. Knudsen,[b] K. J. Måløy[c] and K. P. S. Parmar[a]

[a]Physics Department, Norwegian University of Science and Technology (NTNU), Trondheim, Norway, [b]Physics Department, Institute for Energy Technology (IFE), Kjeller, Norway, [c]Physics Department, University of Oslo (UiO), Oslo, Norway, and [d]Geosciences Rennes, UMR CNRS 6118, Université de Rennes 1, Rennes, France. Correspondence e-mail: davi.fonseca@phys.ntnu.no, jon.fossum@ntnu.no

A study of polydisperse suspensions of fluorohectorite clay in saline solutions is presented. The suspended clay colloids consist of stacks of nanosilicate sheets several tenths of a nanometre thick. They are polydisperse both with respect to the number of stacked nanolayers and with respect to their extension along the sheets. Due to this polydispersity, a spontaneous gravity-induced vertical segregation occurs in the sample tubes and results in the presence of up to four different phases on top of each other. Precise characterization of the phase diagram of the samples as a function of salt concentration and vertical position in the tubes, based on small-angle X-ray scattering data, is presented. The vertical positions of the phase boundaries were monitored by analyzing the eccentricity of elliptic fits to iso-intensity cuts of the scattering images. The intensity profiles along the two principal directions of scattering display two power-law behaviors with a smooth transition between them and show the absence of positional order in all phases.

1. Introduction

Colloidal suspensions of 2:1 clay particles in aqueous salt solutions make ideal model systems for the study of interactions between platelet-shaped particles. Indeed, the particle–particle interaction consists of (i) the van der Waals attraction and (ii) the electrostatic repulsion between the particles' electric double layer (McBride & Baveye, 2002). The extension of the latter repulsion can be easily tuned by changing the electrolyte concentration (Israelachvili, 1992). This complex particle–particle interaction combined with the strong particle anisotropy results in rich phase behaviors. The phase diagram of the monodisperse synthetic 2:1 clay laponite dispersed in saline solution, in particular, has been the subject of much attention (Mourchid *et al.*, 1998; Bonn *et al.*, 1999; Lemaire *et al.*, 2002). Such dispersions are now well known for the existence of a spontaneous nematic arrangement of the platelets at given salt and particle concentrations (Mourchid *et al.*, 1998; Lemaire *et al.*, 2002; van der Beek & Lekkerkerker, 2003).

Another synthetic clay, sodium fluorohectorite (NaFHT), has been found to exhibit interesting phase behavior when suspended in saline solutions. NaFHT presents polydispersity in both particle size and aspect ratio (Kaviratna *et al.*, 1996). In the presence of polydispersity a spontaneous phase segregation occurs in the suspensions (Fossum, 1999; Bates, 1999; van der Kooij *et al.*, 2001), with several phases co-existing in strata. X-ray diffraction studies of such systems (DiMasi *et al.*, 2001) have investigated the clay particles' orientations in these NaFHT–NaCl–H_2O systems, taking advantage of their nano-layered nature. Three distinct gel regions were identified and characterized by differences in orientational order and/or the size of ordered domains. One phase was presented as nematic. Those findings are consistent with visual observations (Fossum *et al.*, 2005), including observations through crossed polarizers: a birefringent region, coinciding with the region exhibiting orientational order (as inferred from the wide-angle X-ray scattering study), was observed. More recently, the existence of an isotropic-to-nematic transition in these systems has been corroborated by MRI studies of anisotropic water self-diffusion (de Azevedo *et al.*, 2007).

However, the corresponding phase diagram has not yet been determined with precision, nor has the orientationally ordered gel phase been fully characterized as nematic. In the present work, synchrotron small-angle X-ray scattering (SAXS) is used to obtain a fine characterization of the phase diagram over a large NaCl concentration range.

2. Experimental method

2.1. Samples

The samples consist of NaFHT crystallites suspended in a saline solution. They were prepared in the following way: lithium fluorohectorite clay was purchased in powder form from Corning Inc. (New York). It was cation-exchanged using NaCl, and then the extra Cl^- ions were removed through dialysis. After drying, the obtained clay crystallites have the nominal chemical formula $Na_{0.6}(Mg_{2.4}Li_{0.6})Si_4O_{10}F_2$.

Several suspensions of such crystallites were subsequently prepared, with a 3 wt% concentration of clay and NaCl concentrations ranging from 0.1 to 25 m*M* (Table 1). After addition of the clay

Table 1
Vertical positions at which SAXS data were recorded for each sample.

Saline concentration (m*M*)	Starting position† (mm)	Step size (mm)	Number of SAXS scans
0.1	0	1	15
0.25	0	1	23
0.5	0	1	23
0.75	0	0.5	45
1.0	0	0.5	45
2.5	1	0.5	45
5.0	1	0.5	45
7.5	1	0.5	45
10	1	0.5	45
25	1	0.5	55

† Above the bottom of the sample.

powder to the saline solution, the suspensions were left shaking overnight; after twelve hours, they were poured into 2 mm diameter capillaries made of quartz glass (Hilgenberg Mark tubes with 0.01 mm wall thickness). They were then allowed to settle for 30 days. After this time, one could observe up to four superimposed phases, as shown in Fig. 1: the phase at the very bottom is opaque; that on top of it is a translucent gel; the third phase observed from the bottom up is a transparent gel; the top phase is a transparent sol.

2.2. Scattering setup

SAXS experiments were performed on the Dutch–Belgian Beamline (DUBBLE) at the European Synchrotron Radiation Facility (ESRF) in Grenoble (France). This beamline provides focused monochromatic radiation with an energy tunable in the range 5–30 keV, corresponding to wavelengths between 0.41 and 2.48 Å. A wavelength of 1.55 Å was chosen for this experiment.

The experimental hutch contains the SAXS camera with a maximum and minimum sample-to-detector distance of 8 and 1.4 m, respectively. The maximum camera length $D = 8$ m was chosen for the whole length of the measurements, so as to investigate length scales as large as possible. Two-dimensional SAXS images were recorded using a two-dimensional multiwire gas-filled detector (Gabriel & Dauvergne, 1982). This detector has an image size of 133× 133 mm with a spatial resolution of 250 ± 5 µm. The beam size that we used had a diameter of ~0.2–0.3 mm and the beam stop was approximately a 5 × 5 mm square. Consequently, for the chosen wavelength λ of 1.55 Å, the q range accessible in the experiment was 0.013–0.33 nm^{-1} [where $q = (4\pi/\lambda)\sin\theta$ and 2θ is the scattering angle], corresponding to probed length scales between 20 and 480 nm. The measurement setup also contains a linear wide-angle X-ray scattering (WAXS) detector based on a curved microstrip glass strip counter. This allowed us to simultaneously record SAXS and WAXS data with a time resolution down to 1 ms per timeframe. The WAXS data will not be discussed in this paper.

In order to avoid repeatedly entering the experimental hutch to change samples, a sample holder containing ten capillaries placed side by side and regularly spaced was employed. The samples were placed in the beam in turn by translating the holder using a remotely controlled horizontal translation stage. Another translation stage allowed control of the vertical position of the sample with respect to the beam.

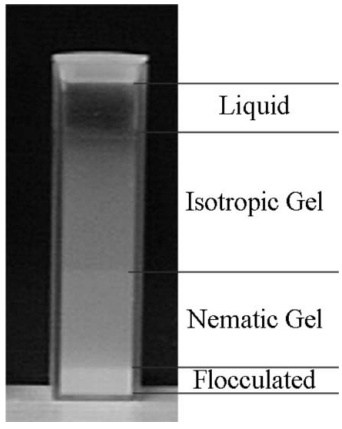

Figure 1
A sodium fluorohectorite sample with a particle concentration of 3 wt% and an NaCl concentration of 4.5 m*M*. The four phases are easily identifiable.

2.3. Experimental protocol

For each sample: (i) a vertical transmission scan was carried out and (ii) SAXS patterns at different heights were collected. Table 1 lists the details of the vertical positions at which SAXS data were recorded for each sample. The liquid phase at the top of the sample tube was not investigated. All SAXS images were recorded with an exposure time of 60 s. They were subsequently corrected for the detector's transfer function and normalized with respect to the sample transmission. Scattering from the empty tubes proved to be negligible compared to the data and therefore no subtraction of the empty tube data was necessary.

3. Data analysis

3.1. Method

Fig. 2 displays examples of SAXS images recorded from the lower and upper gel phases for a salt concentration of 1 m*M*. The data in

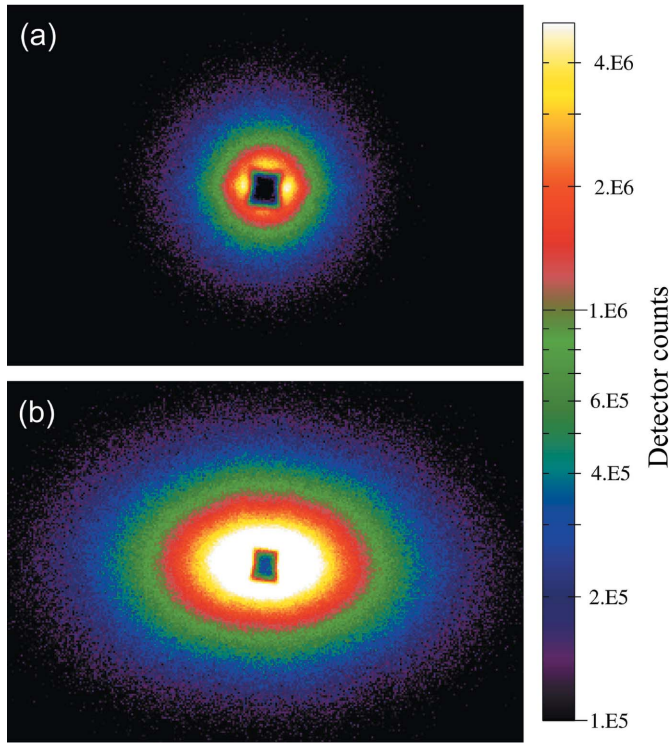

Figure 2
SAXS images recorded in the upper (*a*) and lower (*b*) gel phases. The anisotropic image in (*b*) indicates a preferential orientation of the clay crystallites in the lower phase.

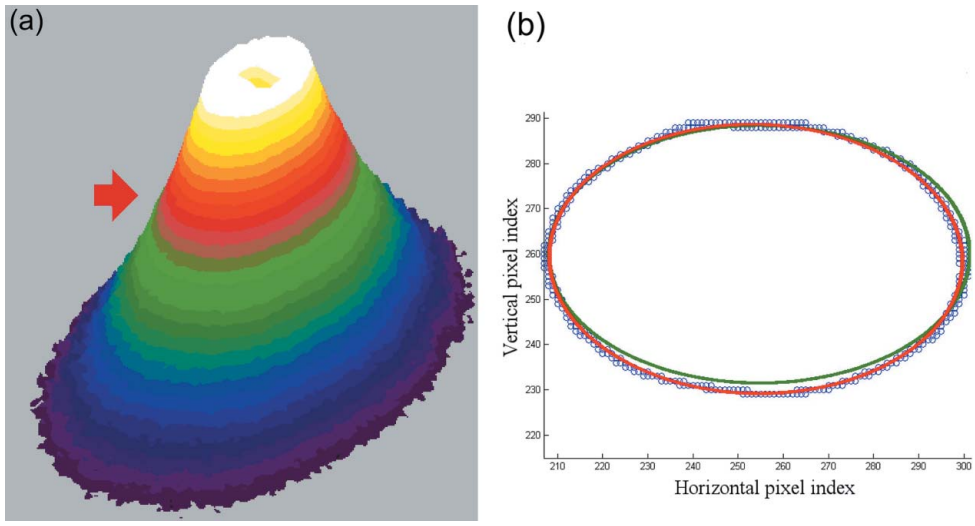

Figure 3
(*a*) A three-dimensional view of a scattering image. The arrow indicates a range that could be used to generate the cloud of points. (*b*) The blue circles represent the cloud of points inside the range of the scattering profile. The green ellipse is the initial guess for the fitting procedure. The red ellipse is the evaluated best fit to the cloud of points.

Fig. 2(*a*) are isotropic, while those displayed in Fig. 2(*b*) are clearly anisotropic, indicating a preferential orientation of the clay crystallites.

Iso-intensity lines of the SAXS images are well described by ellipses. Hence, a custom-made *MATLAB* program was used to fit ellipses to such iso-intensity lines. The fitting procedure is accomplished in the following way. First, a narrow intensity range is selected (Fig. 3*a*), and then the pixels with an intensity that falls in that range are extracted from the two-dimensional SAXS image. Subsequently an ellipse is fitted to the cloud of points defined by the horizontal and vertical coordinates of the selected pixels (Fig. 3*b*). This procedure provides the center of the ellipse, the length of its major axis, a, that of its semi-minor axis, b, and its angle of tilt with respect to the horizontal. From a and b one can calculate the eccentricity, e, where $e = [1 - (b^2/a^2)]^{1/2}$. This procedure was tested at different intensity levels and the fit results were shown to depend only weakly on the intensity range used to obtain them.

The obtained fit parameters can be related to the scattering process as follows: (i) the center of the ellipse is a fine estimate for the position of the direct beam; (ii) the principal axes of the ellipse are related to the orientational ordering of the scattering clay particles; (iii) the eccentricity of the ellipse is a measure of the image's anisotropy: an image with a perfect axial symmetry would yield a value e = 0, while a value closer to 1 denotes a very anisotropic image; and (iv) the angle of tilt of the ellipse is related to the preferential orientation of the scatterers with respect to the laboratory frame.

Finally, one-dimensional intensity profiles of scattering intensity *versus* q along the principal axes of the ellipses were computed. Those profiles were generated by integrating the images over azimuthal angles in 5° wide sectors around each of the principal directions. The resolution of these profiles along the radial direction was set to 250 radial bins.

3.2. Results

3.2.1. Phase diagram. The computed eccentricities were plotted as a function of the vertical position for each sample. From these plots (not shown here) it is readily noticeable that: (i) a region at the bottom part of the sample corresponds to eccentricities spread over a wide range of values, (ii) a region which only contains high eccentricity values is found on top of the latter one, and (iii) the third region from the bottom up contains only low eccentricity values. Note that the fourth (and top) phase observed visually in the highest part of the sample tube was not studied by SAXS, and will not be discussed in what follows. The three regions found from the SAXS data correspond to the three bottom phases observed visually. Since the anisotropy of the scattering images is characteristic of particle orientational ordering, the phases were identified as the sediment, a gel phase with preferential particle ordering and an isotropic gel, respectively.

From these plots for individual samples, a surface plot taking all samples into account was constructed. Since the concentrations used here form a nonregular and nonmonotonic grid, *MATLAB* was used to interpolate the data on a regular grid. Fig. 4(*a*) shows a grayscale view of the surface plot, with salt concentration along the horizontal axis and vertical position along the vertical axis; grayscale intensities denote the eccentricity value at a given point of the parameter space. In this representation, sudden changes in the gray level denote possible phase boundaries. A dark gray zone at the top of the image obviously denotes the isotropic gel phase, since the scattering from that phase is isotropic. On the other hand, the images collected in the gel phase with a preferential orientation of the particles must correspond to high eccentricities, since the characteristic orientational ordering causes a very anisotropic scattering. Therefore, the white zone on the left part of the image, under the region corresponding to the isotropic gel, corresponds to that anisotropic gel.

In order to complete our understanding of the phase boundaries as inferred from the SAXS data, a grayscale image of the transmission data was also made (Fig. 4*b*). Owing to the relatively sharp change in transmission from the sediment to the gel phases, it is easy to identify the sediment. Note that the images of Figs. 4(*a*) and 4(*b*) complement each other; their joint interpretation allows clear definition of the phase boundaries for the sediment, anisotropic gel and isotropic gel. We are left with an unidentified region in the right-hand part of the image, between the regions corresponding to the sediment and to the isotropic gel. That region exhibits moderate attenuation and moderate eccentricity values that vary on a small scale in the parameter space. It also exhibits all possible angles of tilt for the fitted ellipses (tilt-angle data are not shown here).

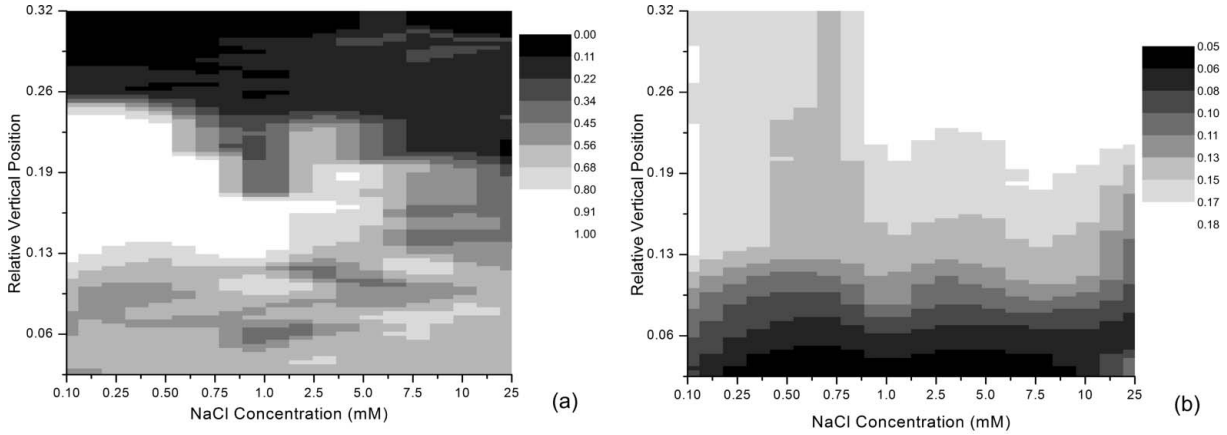

Figure 4
(*a*) Grayscale map for the eccentricity values computed from the SAXS data as a function of the salt concentration and vertical position in the sample tubes. (*b*) As for (*a*), but computed from the transmission data.

Fig. 5 summarizes this phase diagram for the suspensions. Note that the use of the relative vertical position as a vertical axis in Fig. 5 is somewhat unphysical. It can however be related to a more physical parameter such as the particle volume fraction. Indeed, the vertical phase segregation is thought to be related to a vertical gradient in volume fraction, as a consequence of polydispersity. In this sense, the phase diagram in Fig. 5 can be related to better-known phase diagrams of clay colloids in saline solution (that of laponite, for example) as a function of particle volume fraction and ionic strength of the solution. We do not know yet how the relative vertical position in the tube translates into local volume fraction, hence we cannot convert the vertical axis into a volume fraction axis. When Fig. 5 is compared to the two previous estimates of the diagrams, one from visual observation, the other one from WAXS data [see DiMasi *et al.* (2001) and Fossum *et al.* (2005)], it is evident that the main features are consistent. The anisotropic gel found here is the nematic gel phase as identified from WAXS data. Fig. 2(*b*) is a typical SAXS image recorded from this phase; the orientation of the elliptic iso-intensity lines is consistent with the previous WAXS analyses, according to which the platelet-shaped clay particles are standing on

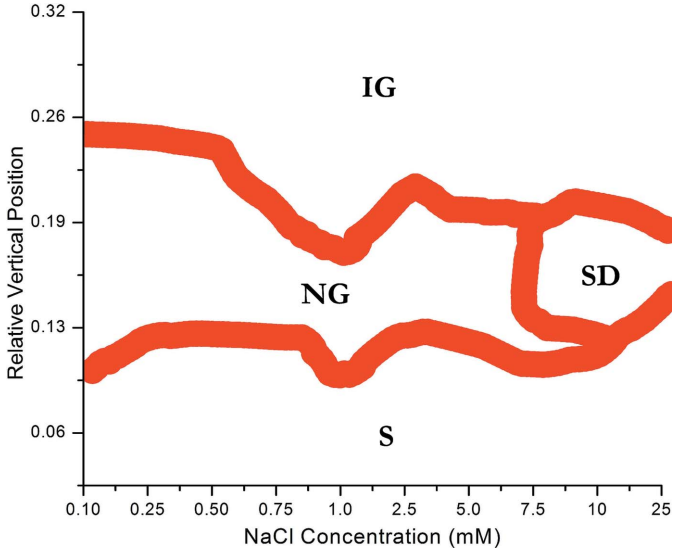

Figure 5
Phase diagram created from the grayscale maps for eccentricity and transmission. The displayed regions are sediment (S), nematic gel (NG), isotropic gel (IG) and a region containing small domains (SD). The line thickness corresponds to the uncertainty on the boundary position.

average with their short dimension along the horizontal (DiMasi *et al.*, 2001). The rightmost region in the diagram (Fig. 4*a*) corresponds to what DiMasi *et al.* (2001) denote as a small nematic domain phase (SD). We believe that this region contains in fact many small nematic regions. On the scale of the scattering volume, this results in SAXS data with a moderate anisotropy, the magnitude and preferential orientation of which are not fixed for the whole region.

Two discrepancies between the current phase diagram and the previous estimates can be spotted. One of them is that the phase boundaries are not exactly at the same vertical position. This is expected since the samples in the different experiments were allowed to settle for unequal times and the phase boundaries are known to change position for several months before they stabilize. The other evident new observation compared to our previous studies concerns the boundary of the two gel phases at low salt concentrations. Its first two points in the previous estimates are much higher than that observed here (around two times higher) with respect to the rest of that boundary. The behavior observed in the present experiment is systematic and is observed for five different concentrations here, whereas it was observed for only two concentrations in the other works. Currently, one may suggest several alternative explanations for this difference and this will be a subject for future work.

3.2.2. Spectra along the principal axes. For a given SAXS image, the scattering intensity as a function of the modulus q of the scattering vector was also plotted along the two principal directions of the image, as determined by the fitting of ellipses to iso-intensity lines. Fig. 6 presents such q plots for a SAXS image in the isotropic phase and another one in the nematic phase of the sample with a saline concentration of 1 m*M*.

The q plots in Fig. 6 appear as consisting of several power-law regimes. This is expected in SAXS data from systems of aggregated particles (Schmidt, 1991). On all plots, a smooth crossover is noticed. It corresponds to a characteristic length scale of ~20 nm. This could be related to the average thickness of the stacks of clay platelets, which is the only characteristic length of the particles that can be probed in the q range investigated with SAXS. Another interpretation for this crossover scale would be that small nematic domains exist locally in the two gel phases, with a typical particle-to-particle distance of around 20 nm. The crossover is smooth due to polydispersity in the particle thicknesses. Note that the characteristic length scale does not correspond to a regular periodicity in the mesostructure, since no peak is visible in the data at the corresponding q value. Hence, none of the phases exhibits positional order on the length scales probed by the SAXS experiment. In particular,

Table 2
Power-law exponents determined from Fig. 6.

	Slope left of crossover	Slope right of crossover
Nematic along semi-major axis	−2.2 ± 0.2	−2.8 ± 0.1
Nematic along semi-minor axis	−2.3 ± 0.1	−2.9 ± 0.1
Isotropic along semi-major axis	−2.2 ± 0.1	−2.4 ± 0.1
Isotropic along semi-major axis	−2.5 ± 0.1	−2.4 ± 0.2

the lower gel phase is ordered with respect to particle orientations but not to positions.

The values for the exponents of the power laws, as estimated from slopes in the log–log plots in Fig. 6, are presented in Table 2. We notice that at higher q values the slopes seem to approach −4, possibly indicating crossover into the Porod regime as the probed length scales become smaller than the crossover length scale. We also notice that at lower q values the slopes approach −2. This is expected for monodisperse platelets with no correlations between particle positions and orientations, either (i) nematically oriented, provided that q is pointing along the normal to the platelets, or (ii) randomly oriented (Ramsay, 1990). For nematically oriented monodisperse platelets with no correlations between positions and orientations, a slope of −3 is expected when q points perpendicular to the short plate direction (Ramsay, 1990). Note that our observations in terms of power-law exponents may be influenced by the fact that our platelets are not monodisperse, and that positions and orientations of particles may be correlated.

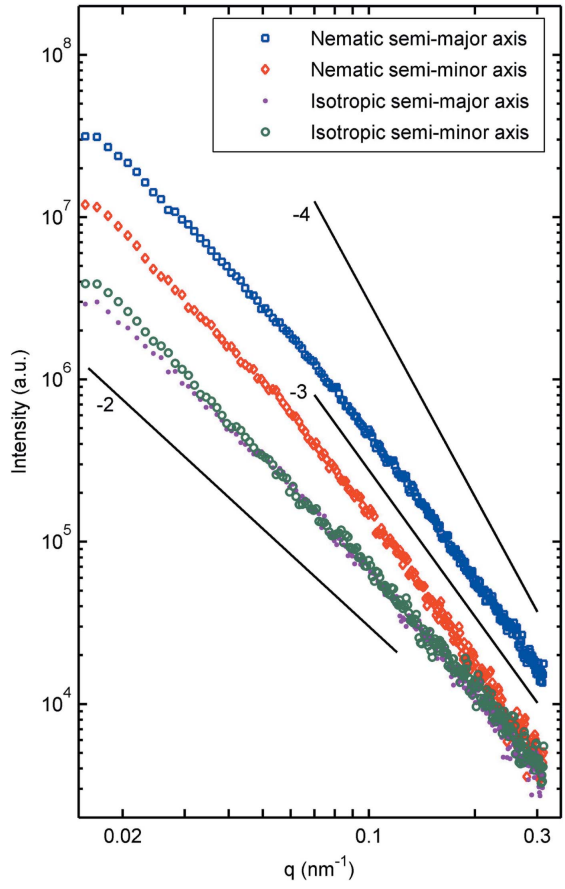

Figure 6
Integrated intensity plots as a function of the modulus of the scattering vector, q, along the principal axes of the ellipse, for a point in the isotropic phase and also for a point in the nematic phase. The smooth crossover is positioned at a q value corresponding to a length scale of about 20 nm. The solid lines denote reference slopes.

4. Conclusion

SAXS experiments have allowed a precise characterization of the phase diagram of suspensions of sodium fluorohectorite platelet-shaped particles in saline solutions. The characterization was done based on transmission data and on two-dimensional SAXS images.

Ellipses were fitted to iso-intensity lines of the SAXS images. The phase boundaries were obtained through joint analysis of the transmission data and of results for the eccentricities and tilt angles of the ellipses. Among the different phases observed, one is a gel phase exhibiting a high degree of orientational order, while another is an isotropic gel. This phase diagram is consistent with our previous estimates using other approaches. Moreover, plots of the integrated intensities *versus* the modulus of the scattering vector along the principal axes of the ellipses for both gel phases exhibit power-law behaviors with a smooth crossover at a characteristic length scale that may correspond to the typical particle thickness, and exponents that approach those of well known configurations at the lower and higher q values. These q plots confirm that no positional order exists in any of the phases.

X-ray scattering techniques have proved to be appropriate for discriminating between different phases in these samples. Future work concerns further understanding of the differences between the different phases, in terms of the geometry of the porous space between the particles (Knudsen *et al.*, 2004), focusing on the power-law behavior of the q plots. The ultimate goal is to understand the underlying mechanisms responsible for the formation of the different phases.

The authors acknowledge the European Synchrotron Radiation Facility for provision of synchrotron radiation facilities and we would like to thank Dr Igor Dolbnya for assistance in using beamline BM26B. The two anonymous referees are also acknowledged for helping to improve the manuscript. This work has received partial financial support from the Research Council of Norway (RCN) through the NANOMAT Program: RCN project numbers 152426/431, 154059/420 and 148865/432, as well as through 138368/V30 and SUP154059/420.

References

Azevedo, E. N. de, Engelsberg, M., Fossum, J. O. & de Souza, R. E. (2007). *Langmuir*, **23**, 5100–5105.
Bates, M. A. (1999). *J. Chem. Phys.* **111**, 1732–1736.
Beek, D. van der & Lekkerkerker, H. N. W. (2003). *Europhys. Lett.* **61**, 702–707.
Bonn, D., Tanaka, H., Kellay, H., Wegdam, G. & Meunier, J. (1999). *Langmuir*, **15**, 7534–7536.
DiMasi, E., Fossum, J. O., Gog, T. & Venkataraman, C. (2001). *Phys. Rev. E*, **64**, 61704.
Fossum, J. O. (1999). *Physica A*, **270**, 270–277.
Fossum, J. O., Gudding, E., Fonseca, D. d. M., Méheust, Y., DiMasi, E., Gog, T. & Venkataraman, C. (2005). *Energy*, **30**, 873–883.
Gabriel, A. & Dauvergne, F. (1982). *Nucl. Instrum. Methods*, **201**, 223–230.
Israelachvili, J. (1992). *Intermolecular and Surface Forces*. London: Academic Press.
Kaviratna, P. D., Pinnavaia, T. J. & Schroeder, P. A. (1996). *J. Phys. Chem. Solids*, **57**, 1897–1906.
Knudsen, K. D., Fossum, J. O., Helgesen, G. & Haakestad, M. W. (2004). *Physica B*, **352**, 247–258.
Lemaire, B. J., Panine, P., Gabriel, J. C. P. & Davidson, P. (2002). *Europhys. Lett.* **59**, 55–61.
McBride, M. B. & Baveye, P. (2002). *Soil Sci. Soc. Am. J.* **66**, 1207–1217.
Mourchid, A., Lecolier, E., van Damme, H. & Levitz, P. (1998). *Langmuir*, **14**, 4718–4723.
Ramsay, J. D. F. (1990). *J. Chem. Soc. Faraday*, **86**, 3919–3926.
Schmidt, P. W. (1991). *J. Appl. Cryst.* **24**, 414–435.
Van der Kooij, F. M., van der Beek, D. & Lekkerkerker, H. N. W. (2001). *J. Phys. Chem. B*, **105**, 1696–1700.